remote sensing

MDPI

Article

Comparison of Assimilating Clear and All-Sky GOES-16 ABI Radiance in a Convective-Scale Model to Improve the Forecast of an MCS Event

Lijian Zhu [1,2], Ming Xue [2,*], Hong Li [1] and Jingyao Luo [1]

[1] Shanghai Typhoon Institute, The China Meteorological Administration, Shanghai 200030, China; zhulj@typhoon.org.cn (L.Z.); lih@typhoon.org.cn (H.L.); luojy@typhoon.org.cn (J.L.)
[2] Center for Analysis and Prediction of Storms, School of Meteorology, University of Oklahoma, Norman, OK 73072, USA
* Correspondence: mxue@ou.edu

Highlights

What are the main findings?

- Clear-sky radiances mainly adjust the near-storm environment, whereas all-sky radiances produce more realistic cloud, cold pool, and storm circulation analyses.
- All-sky assimilation shows larger and longer-lasting forecast improvements, particularly for cloud structure, radar reflectivity, and precipitation.

What are the implications of the main findings?

- Cloud-affected infrared radiances provide valuable storm-scale information for initializing rapidly evolving convective systems.
- Rapid-update all-sky infrared radiance assimilation improves the analysis and short-range forecast of convective weather in a convective-scale model.

Abstract

Geostationary infrared observations provide frequent, spatially continuous information on rapidly evolving convective systems. This study assimilates clear-sky and all-sky Channel 10 brightness temperatures (BTs) from GOES-R Advanced Baseline Imager (ABI). The impacts on the analysis and short-range forecast of a continental meso-scale convective system (MCS) are compared. The implementation is achieved in a convection-permitting model using a 5 min cycling ensemble Kalman filter (EnKF) framework. A quality control procedure is developed to enable the effective assimilation of clear-sky ABI observations. Results show that clear-sky assimilation partially removes spurious background clouds and adjusts temperature and moisture in the near-storm environment. All-sky assimilation substantially improves the analyzed cloud field, produces stronger in-storm thermodynamic and dynamical increments, as well as directly constrains hydrometeor variables. In addition, assimilating all-sky observations reduces errors of analyzed surface temperature and humidity by over 25%. Forecast verification further indicates that all-sky assimilation provides more persistent forecast improvements in terms of BT and reflectivity quantities than clear-sky assimilation does. Both clear-sky and all-sky assimilations improve the spatial coverage and intensity of accumulated precipitation, but assimilating all-sky observations produces substantially larger FSS gains (0.163–0.380 versus 0.02–0.13).

Keywords: all-sky infrared radiance; data assimilation; advanced baseline imager

Check for updates

Academic Editor: Filomena Romano

Received: 21 August 2026
Revised: 8 October 2026
Accepted: 13 October 2026
Published: 21 October 2026

Copyright: © 2026 by the authors. Licensee MDPI, Basel, Switzerland. This article is an open access article distributed under the terms and conditions of the Creative Commons Attribution (CC BY) license.

1. Introduction

Severe convective weather, including meso-scale convective systems (MCSs), severe thunderstorms, and associated extreme precipitation, causes substantial hazards worldwide annually. Accurate prediction of these events remains challenging in convection-permitting numerical weather prediction (NWP). Forecast errors arise from nonlinear interactions among the pre-convective environment, cloud microphysical processes, and storm-scale circulations [1–3]. Small errors in the initial states, particularly in moisture and convective-scale structures, can grow rapidly through moist processes and substantially affect subsequent forecasts [4,5]. Therefore, improving both the storm environment and the existing convective system in the initial condition through advanced data assimilation (DA) is essential for short-range convective prediction [3,6].

Modern geostationary imagers provide infrared (IR) observations at spatial and temporal resolutions suitable for convective-scale DA. Over the past years, IR radiances have been successfully assimilated under clear-sky in global and regional NWP systems to improve the analyses of humidity, temperature and wind fields [7–10]. More recently, the assimilation of clear-sky IR radiances has been extended to convection-permitting models and has shown positive impacts on the forecasts of convective systems and heavy rainfalls [11–16]. However, clear-sky radiance (CSR) DA requires stringent cloud detection and quality control procedures that reject many observations in cloudy and precipitating regions. Consequently, direct observational constraints on clouds and precipitation are largely absent where they are most needed for convective-scale initialization.

All-sky radiance (ASR) assimilation attempts to address this limitation by jointly assimilating clear and cloud-affected observations. When supported by the DA systems, it can also update hydrometeor and microphysical variables alongside the conventional ones. Numerous studies have already demonstrated the potential impacts of all-sky IR assimilation on tropical cyclones, isolated thunderstorms, heavy rainfall, and MCSs within convection-permitting NWP models using advanced DA approaches [17–26].

Direct comparisons of CSR and ASR assimilation have begun to quantify the added value of cloud-affected IR radiances. For example, in the European Center for Medium-Range Weather Forecasts (ECMWF) global system, all-sky assimilation of Infrared Atmospheric Sounding Interferometer (IASI) water vapor radiances was reported to have larger improvements in the tropics than CSR assimilation [27]. Comparisons of Advanced Himawari Imager (AHI) assimilation in the mesoscale and global systems of the Japan Meteorological Agency (JMA) showed that ASR assimilation greatly increased observational coverage and improved moisture analyses and forecasts of middle- and upper-troposphere [21,28]. More recent regional studies have reported similar advantages for monsoon rainfall and tropical cyclones [29,30]. At convection-permitting resolution, Xu et al. [31] assimilated AHI clear-sky and all-sky observations in a 3 h interval using a variational approach, and improved the prediction of a severe storm over North China. He et al. [32] further showed that hourly assimilation of all-sky Fengyun-4A (FY-4A) Advanced Geostationary Radiation Imager (AGRI) radiances outperformed clear-sky assimilation in representing clouds and forecasting precipitation for a warm sector heavy rainfall event over South China.

These studies establish the potential value of ASR assimilation, but the comparison with CSR assimilation remains sensitive to model resolution, cycling frequency, weather regime, and so on. Much of the existing evidence comes from global systems, month-long regional experiments, tropical cyclones, or convection-permitting experiments with hourly or longer cycling intervals. Although recent studies have begun to compare CSR and ASR assimilation at convection-permitting resolution, such comparisons remain limited for rapidly evolving convective systems under rapid-update DA systems. Building on the

GOES-R ABI all-sky assimilation framework developed in our previous study [22], the present study implements a clear-sky assimilation scheme within the same convection-permitting GSI-based EnKF system. The impact of assimilating clear-sky and all-sky ABI water vapor channel observations is systematically evaluated for a continental MCS case. Clear-sky and all-sky ABI observations are assimilated using the same model configuration, cycling period, and ensemble framework, thereby providing a controlled comparison that isolates the added value of cloud-affected radiances. The experiments are designed to address the following two questions. First, to what extent can CSR assimilation improve the MCS analysis and forecast? Second, how much additional benefit can be obtained by assimilating IR radiances within cloudy regions?

The remainder of this paper is organized as follows. Section 2 describes the model setups and experimental design. Section 3 presents the quality-control results for clear-sky ABI assimilation. Section 4 compares the analysis and forecast impacts of the clear-sky and all-sky experiments. Discussion and Conclusions are provided in Sections 4 and 5, respectively.

2. Model Setups and Experiment Design

In this study, the Advanced Research version of the Weather Research and Forecasting (WRF-ARW) [33] Model, version 3.8.1, is used as the forecast model. The DA system uses the GSI-based EnKF system developed and enhanced by the Center for Analysis and Prediction of Storms (CAPS). The Community Radiative Transfer Model (CRTM) [34] version 2.3.1 is employed to simulate both clear-sky and all-sky infrared BTs. The all-sky CRTM calculations account for the radiative effects of model-resolved clouds and hydrometeors.

The case used in this study is a continental mesoscale convective system that developed over the central U.S. plains on 12–13 July 2018, and was previously examined by Zhu et al. [22] and Kong et al. [35]. The model configuration generally follows Zhu et al. [22]. The single model domain contains 300 × 300 horizontal grid points centered at 43.3°N, 96.7°W, with a grid spacing of 3 km and 50 vertical layers in total. A 40-member ensemble is created using time-lagged forecasts from the Short-Range Ensemble Forecast (SREF) system and the analysis fields from the North American Mesoscale (NAM) forecast system valid at 1800 UTC 12 July, and is integrated forward for 3 h to spin up convective structures. The initial and boundary conditions are generated by subtracting the SREF control run from the selected SREF members and adding these perturbations to the 1800 UTC NAM analysis. Specifically, the boundary conditions are updated hourly. All ensemble members utilize the same parameterization schemes, including the double-moment Thompson microphysics scheme [36], the Yonsei University (YSU) scheme [37], the Rapid Radiative Transfer Model for General Circulation Models (RRTMG) for longwave and shortwave radiation [38] and the Noah land surface model [39].

In this study, only ABI Channel 10 (7.3 μm) is assimilated following Zhu et al. [22]. ABI channel 10 is relatively sensitive to the moisture and temperature in the lower-to-middle troposphere. Assimilating observations from a single channel also avoids inter-channel observation-error correlations. To examine the different impact of assimilating clear-sky and all-sky ABI radiance on the target MCS analysis and forecast, a control experiment and two data assimilation experiments were conducted separately. The control experiment (referred to as "CTRL") assimilates no observations and continues the 2 h ensemble forecasts from 2100 UTC to 2300 UTC, 12 July. The first DA experiment assimilates clear-sky BTs from ABI channel 10 over the same period every 5 min (referred to as "CLRSKY"), while the second assimilates all-sky channel 10 BTs instead (referred to as "ALLSKY"). Deterministic and ensemble forecasts were then run from 2300 UTC, 12 July, to 0300 UTC, 13 July, initialized by either the ensemble mean or individual members of each experiment.

In both DA experiments, clear-sky ABI observations are thinned to a resolution of 6 km and cloudy observations are assimilated without thinning in the ALLSKY experiment. This adaptively thinning strategy can reduce computational costs and partly mitigate potential correlated observation errors. The horizontal and vertical localization radius are set to 30 km and 4 scaled heights, respectively, consistent with the settings used by Zhu et al. [22]. To maintain ensemble spread, the relaxation-to-prior perturbation (RTPP) [40] covariance inflation method is used with an inflation parameter of 0.8 following Zhang et al. [18]. Specifically, the adaptive observation-error inflation (AOEI) [41] approach is adopted as the observation-error model for all-sky assimilation; for clear-sky data, the observation error is set to a constant value of 3 K following Zhang et al. [18] and Zhu et al. [22]. In addition, a fixed-value bias correction (BC) scheme similar to Zou et al. [7] and Cintineo et al. [42] is used in this study to correct systematic errors. Given the short duration of this specific case, the simulated clear-sky observations were bias corrected using the average bias estimated from three days of clear-sky departures (−0.31 K). Bias correction was not applied to the cloudy observations considering the rapid variation in bias error characteristics in cloudy regions. The state variables updated in CLRSKY experiment include 3D wind fields, potential temperature, and water vapor mixing ratio, while the ALLSKY experiment also updates the mixing ratios of cloud water, cloud ice, rainwater, snow, and graupel (e.g., q_c, q_i, q_r, q_s, q_g).

3. Quality Control for Clear-Sky Data Assimilation

Quality control (QC) is essential for clear-sky satellite radiance assimilation because cloud contamination and large observation operator errors can introduce strongly non-Gaussian innovations. In the CLRSKY experiment, only pixels identified as clear-sky in both the observations and the model background are assimilated. A strict QC procedure based on the EnKF framework is developed.

1. Observations with Channel 10 BTs outside the physical range of 50–550 K are rejected.
2. Observations over lakes, other water bodies, snow-covered surfaces, and coastal boundaries are excluded.
3. Observed pixels with channel 10 BTs below 250 K are classified as cloud-affected and rejected following Johnson et al. [24] and Degelia et al. [43].
4. Observations are rejected if the ensemble-mean total hydrometeor content exceeds 0.1 kg m^{-2}.
5. Observations are rejected when the magnitude of the ensemble-mean innovation, $|y - H(\bar{x})|$, exceeds 5 K, a threshold comparable to that adopted by Zou et al. [7].
6. Observations are rejected if the magnitude of the member-specific innovation, $|y - H(x)|$, exceeds three times the prescribed clear-sky observation error for any ensemble member (i.e., 3 K).

The QC thresholds were selected based on both empirical testing and previous studies. Because the QC procedure consists of several successive and partially overlapping checks, the total number of assimilated observations is expected to be relatively insensitive to modest changes in any single threshold.

Figure 1a,b show the spatial distributions of observations minus background simulations (O–B, hereafter referred to as innovations) at the first analysis time (2100 UTC) for the ALLSKY and CLRSKY experiments, respectively. Because of both the deficiencies in microphysics parameterizations and the uncertainties in the initial conditions, a noticeable mismatch between the observed and simulated storms is observed, particularly for the convective system over Minnesota. Large BT differences between the observations and simulations are therefore found, with absolute innovations frequently exceeding 20 K (Figure 1a). The ALLSKY experiment retains these large innovations, while the CLRSKY

experiment effectively removes them. The retained innovations are relatively small and more uniformly distributed, with most values confined within ±5 K.

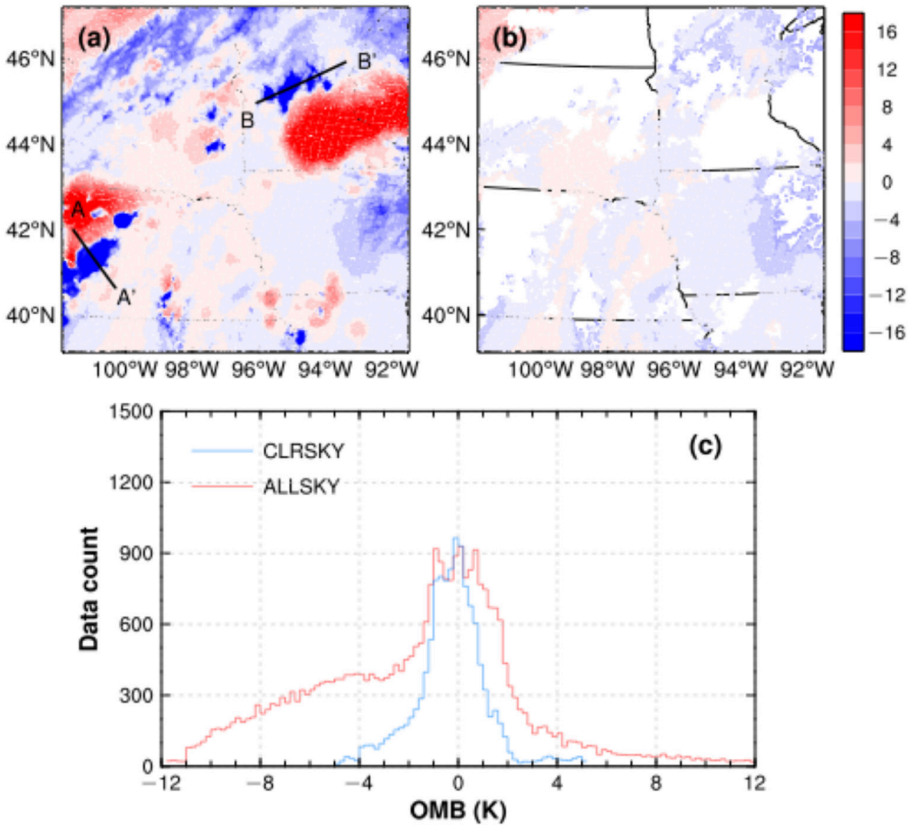


Figure 1. Spatial distributions of the ABI channel 10 innovations (O−B) assimilated at 2100 UTC in (**a**) ALLSKY and (**b**) CLRSKY, and (**c**) frequency distributions of the bias-corrected innovations in ALLSKY (red) and CLRSKY (blue).

Figure 1c shows the frequency distributions of the bias-corrected ABI Channel 10 innovations from ALLSKY and CLRSKY. ALLSKY exhibits a skewed (or a flat-tail) distribution of innovations. This is mainly because no data thinning is applied to cloudy observations in ALLSKY, allowing a larger number of cloud-affected radiance with negative innovations to be kept. Despite the fact that such non-Gaussian characteristics may violate the fundamental Gaussian error assumption underlying the EnKF, their impacts can be partially mitigated through observation-error inflation strategy. In contrast, the innovation distribution in CLRSKY more closely resembles a Gaussian distribution, consistent with the intended effects of the QC and BC procedures. However, it is noteworthy that a small residual bias (~−0.4 K) remains in CLRSKY after QC and BC. Given the rapid error growth and strong nonlinearities inherent at the convective scale, this magnitude is considered acceptable in this study. Nevertheless, the presence of systematic bias suggests that more advanced bias correction approaches are needed (e.g., [28,44–46]).

4. Results

4.1. Observation-Space Diagnostics

The numbers of assimilated observations, the domain-averaged mean biases, root-mean-square innovations (RMSIs) and ensemble spreads of ABI channel 10 BTs are shown in Figure 2. We note that the verification is carried out over observations being assimilated in each experiment. The purpose of these diagnostics is to assess the cycling stability and internal consistency of each EnKF configuration under clear-sky and all-sky conditions.

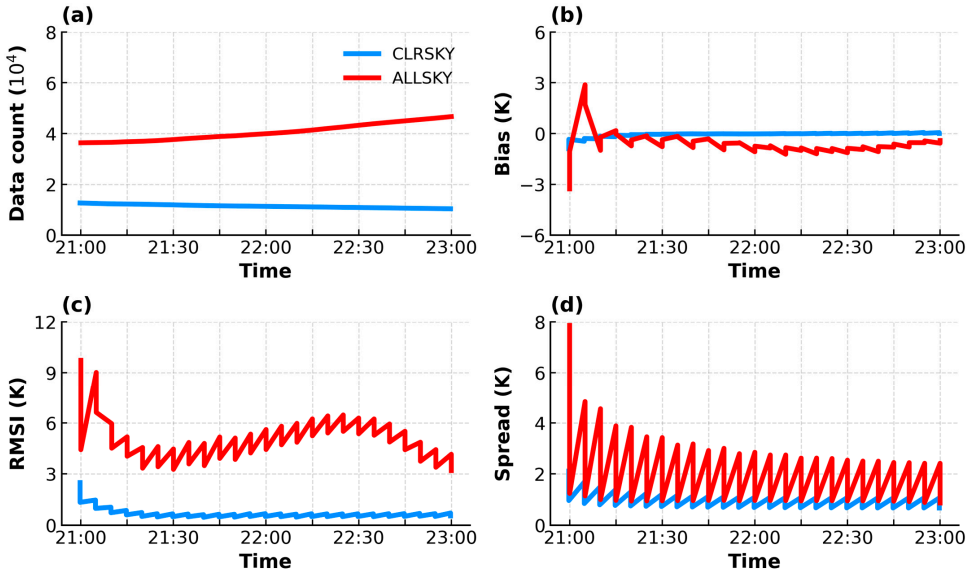


Figure 2. Time series of assimilated observation numbers (**a**), domain-averaged ABI channel 10 BT biases (**b**), RMSIs (**c**) and ensemble spreads (**d**) during the 2 h EnKF period for experiment CLRSKY and ALLSKY, respectively.

ALLSKY assimilated approximately 37,000 observations during the initial cycles, and about 47,000 by 2300 UTC as the MCS becomes more organized (Figure 2a), while the number of observations assimilated by CLRSKY is slightly decreased. The additional observations in ALLSKY provide more constraints within and around the convective systems.

Both experiments show systematic adjustments in observation space during the assimilation cycles (Figure 2b,c). In CLRSKY, both O−B and O−A biases remain small and close to zero after the initial several cycles, while the corresponding RMSIs decrease form 3 K to below 1 K. In ALLSKY, the posterior RMSI remains above 3 K, and the bias remains between −1 and 0 K after the initial adjustment. The larger departures reflect the inclusion of cloud-affected observations with greater cloud position, microphysical, and radiative transfer uncertainties. The ensemble spreads are also well maintained during the cycling period (Figure 2d). The spread in ALLSKY is consistently about three times that in CLRSKY, suggesting the greater uncertainty in simulated BTs under cloudy conditions. These results indicate relatively stable cycling behavior in both configurations.

To more directly compare the different impacts of assimilating clear and all-sky radiances on the analyzed cloud features, we present the observed and simulated ABI Channel 14 BTs from CTRL, CLRSKY, and ALLSKY experiments after final analysis at 2300 UTC. Observations from ABI channel 14 were not assimilated and therefore provided an independent measure of the analyzed high cloud tops and deep convective structures.

CTRL shows widespread convection and tends to overestimate the overall cloud coverage. CLRSKY provides an improved representation in clear-sky regions compared to CTRL and also partly reduces the spurious clouds, particularly those near cloud edges. These improvements occurred even though cloudy observations were excluded and hydrometeor variables were not updated. The influence therefore results indirectly from the ensemble-derived covariances between clear-sky radiances and the surrounding model states. Nevertheless, substantial cloud-related errors remain in CLRSKY. In contrast, ALLSKY reproduces the observed BTs more closely than CTRL and CLRSKY. The locations and spatial distributions of the two major convective systems closely match the observations, and the cold cloud-top regions are realistically represented (Figure 3d). In addition, the spurious convection evident in CTRL and CLRSKY is substantially reduced. These suggest that the assimilation of all-sky infrared radiances effectively improves the analysis of cloud

and convective structures, leading to a more accurate depiction of MCS organization, and cloud-top characteristics.

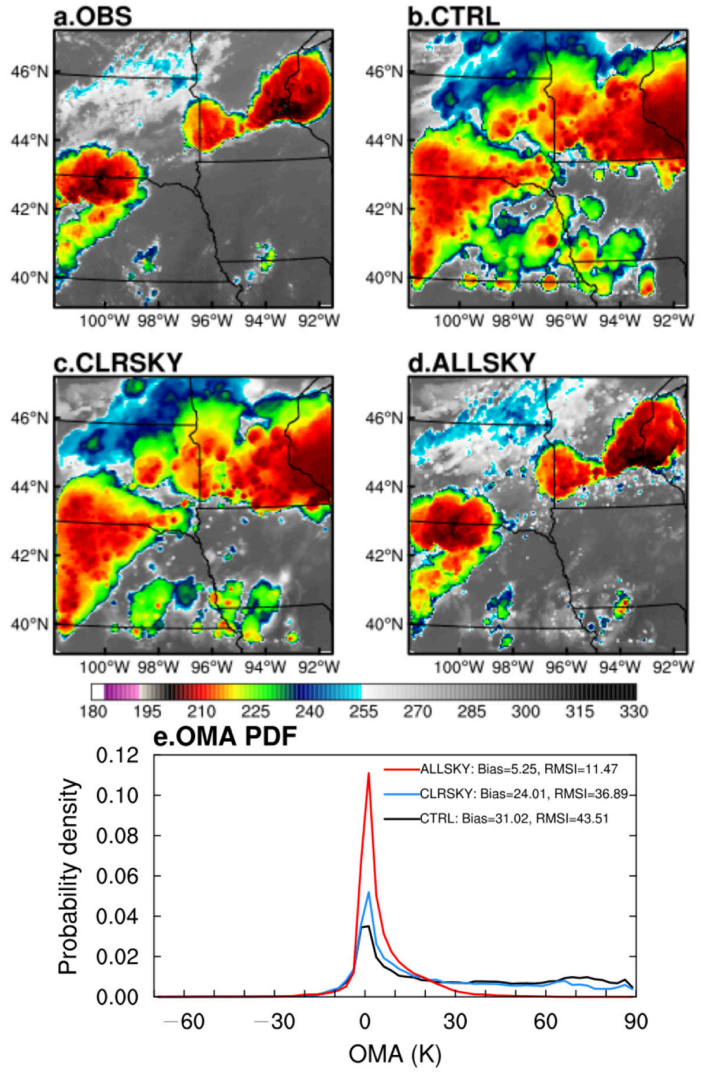


Figure 3. ABI Channel 14 brightness temperatures (K) at 2300 UTC, the final analysis time, for (**a**) observations and simulations from (**b**) CTRL, (**c**) CLRSKY, and (**d**) ALLSKY. (**e**) Corresponding probability density functions (PDFs) of ABI Channel 14 O-As (K) for three experiments. The simulated brightness temperatures were calculated from the ensemble-mean analyses.

The probability density functions (PDFs) at final analysis show that CLRSKY moderately narrows Channel 14 O−A distribution, reducing the bias and RMSI from 31.0 K and 43.5 K to 24.0 K and 36.9 K, respectively. ALLSKY produces a distribution strongly concentrated near zero and reduces the bias and RMSI to 5.25 K and 11.47 K.

4.2. Impacts on Model States

To investigate how clear-sky and all-sky ABI radiance assimilation modifies the model states, vertical cross sections of analysis increments in water vapor mixing ratio (qv), temperature, and wind fields are examined at 2100 UTC, the first analysis time. Two typical cross sections (AA′ and BB′; as shown in Figure 1a) are chosen. Both sections pass through the observed cloudy regions with large negative innovations, but their background conditions are notably different. AA′ is in a partially cloudy background where more than half of the background members are cloudy, while BB′ is in a clear-sky background where all ensemble members are identified as cloud-free. AA′ and BB′ serve as illustrative

examples to examine the local response of all-sky DA and how it depends to different background conditions.

For the AA′ cross section, CLRSKY (Figure 4a) produces only weak analysis increments as most in-storm observations are rejected. The positive q_v increments are generally below 0.4 g kg^{-1} and are mainly confined to the middle troposphere. Weak negative temperature increments are observed at lower levels, whereas wind increments remain small throughout the cross section. In contrast, ALLSKY generally produces substantially larger analysis increments in both thermodynamic and dynamic variables. As is shown, the positive q_v increments reach approximately 1 g kg^{-1} within the observed in-storm regions (Figure 4b), and the magnitude of the temperature increments also increases from 0.3 K in CLRSKY to nearly 1 K in ALLSKY. In ALLSKY, negative temperature increments occur mainly near the cloud top and below the cloud base, while positive increments are within the cloudy layer. The cooling near the cloud top is consistent with latent heating related to the condensation and other microphysical processes in active deep convection [47]. ALLSKY also produces much larger wind increments than CLRSKY does, with enhanced upward motion extending from the lower to the upper troposphere. Such dynamically coupled increments benefit the vertical moisture transport and the internal circulation of the MCS.

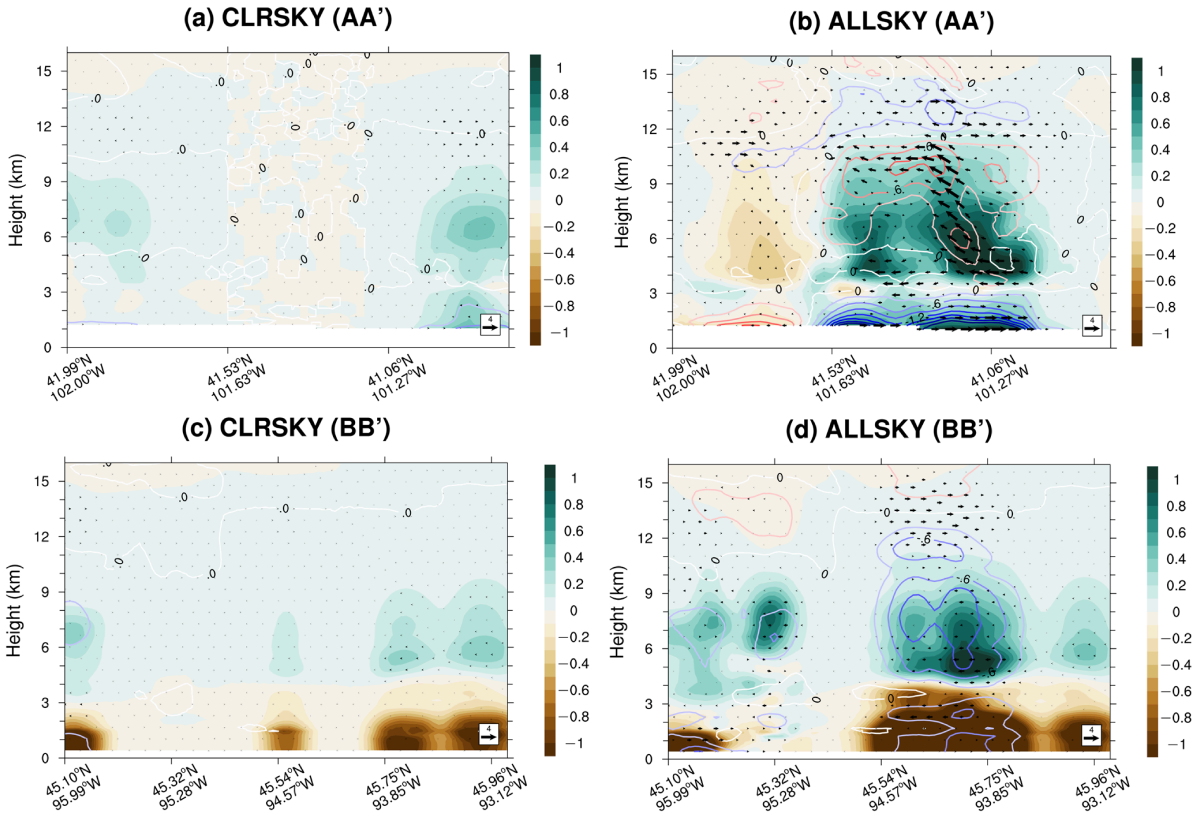


Figure 4. Vertical cross sections of analysis increments in water vapor mixing ratio (shading; g kg^{-1}), temperature (contours; K), and wind (vectors; m s^{-1}) at the first analysis time of 2100 UTC from (**a**,**c**) CLRSKY and (**b**,**d**) ALLSKY for section (**a**,**b**) AA′ and (**c**,**d**) BB′.

A different response is observed in the BB′ cross section. In this case, both CLRSKY and ALLSKY show similar vertical dipole structure in the q_v increments, characterized by mid-level moistening and low-level drying (Figure 4c,d). However, the magnitude of the increments in ALLSKY is much larger. The positive moisture increments are concentrated between approximately 4 and 8 km, while widespread negative temperature increments occur from the lower to middle troposphere. The combined mid-level moistening and cooling increases relative humidity and creates a more favorable thermodynamic environment for

subsequent cloud formation. Because the background contains little or no simulated cloud signal, the assimilation has limited ability to directly rebuild the missing cloud structures. Because of the relatively weak correlation between IR BT and wind fields under clear-sky background, neither experiment produces noticeable wind increments.

These contrasting responses can be understood in terms of the differences in the background error covariances. When clouds are already represented in the background, the background error covariance somehow captures the flow-dependent characteristics within the convective regions. Therefore, all-sky assimilation is able to improve the internal thermodynamic structure of the existing convection and produces stronger dynamically balanced increments. When clouds are missing in the background, EnKF updates model states using the clear-sky background error covariances. In this case, all-sky assimilation acts primarily by reconstructing a favorable thermodynamic environment that facilitates subsequent convection development. Nevertheless, the additional information from cloud-affected infrared radiances enables stronger adjustments on the model variables within and around cloudy regions than clear-sky assimilation does.

We further compare the average vertical profiles of five hydrometeor species among CTRL, CLRSKY, and ALLSKY in the observed cloudy region at the final analysis time (Figure 5). The results also reveal different responses of hydrometeor species to clear and all-sky ABI assimilation. Although the hydrometeor variables were not updated in CLRSKY, their distributions can be modified indirectly through the adjustments to the thermodynamic and dynamical fields. CLRSKY increases cloud water (q_c) and snow water (q_s) relative to CTRL, implying a moister environment in the middle and upper troposphere that favors condensation and ice-phase deposition. However, the lack of corresponding dynamical support within the mature convective cores may have limited the conversion of q_c and q_s into rainwater (q_r) and graupel (q_g), consistent with the concurrent decreases in q_r and q_g.

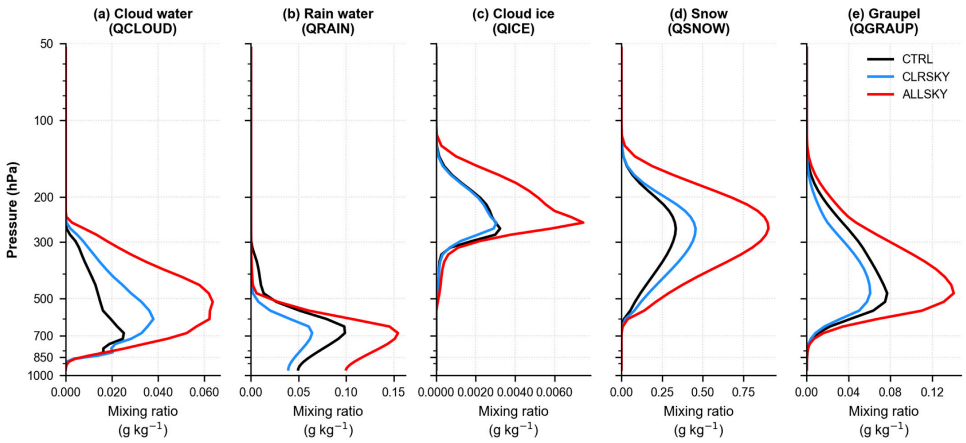


Figure 5. Vertical profiles of the ensemble-mean mixing ratios (g kg^{-1}) of cloud water (QCLOUD), rainwater (QRAIN), cloud ice (QICE), snow (QSNOW), and graupel (QGRAUP) averaged over the observed cloudy regions for CTRL (black), CLRSKY (blue), and ALLSKY (red) at the final analysis time. The cloudy region is defined by observed ABI Channel 10 BTs less than 250 K.

In ALLSKY, the mixing ratios of all five hydrometeor species generally increase within their primary vertical layers. Because cloudy IR BTs are particularly sensitive to upper-level ice-phase particles, assimilating additional cloudy observations provide more direct constraints on q_i and q_s. The increases in upper-level q_i and q_s are consistent with the colder cloud tops shown in Figure 3 and indicate deeper anvil and stratiform cloud structures of the MCS. While the enhanced q_g is likely a result of more active riming progress. For liquid-phase particles, ALLSKY further increases q_c in the mixed-phase layer, providing a greater supply of supercooled liquid water. Compared with CTRL, ALLSKY also retains more q_r at

lower levels but less above approximately 600 hPa, which probably suggests more efficient sedimentation and the melting of ice-phase precipitation. These results demonstrate that all-sky ABI assimilation provides additional constraints on storm-scale cloud and microphysical structures that are unavailable from clear-sky observations. However, due to the lack of independent three-dimensional observations, the extent to which the assimilation improves the vertical structure of the MCS remains unclear.

The assimilation of ABI BTs also modifies the near-surface environment, which also influences the prediction of the target MCS. The ensemble mean of CTRL shows a weak and misplaced cold pool structure, together with weak low-level convergence ahead of the convective system (Figure 6g). Verification against ASOS observations indicates that CTRL has a warm bias (2.08 °C) and a dry relative humidity bias (5.57%), with RMSEs of 4.11 °C and 14.04%, respectively (see Table 1). CLRSKY slightly improves the near-surface environment, reducing the bias and RMSE of 2 m temperature to 1.78 and 3.71 °C, respectively. It is seen that a slightly stronger cold pool is found over data-rich regions, including northern South Dakota and central Minnesota. However, the corresponding improvement in near-surface humidity and wind fields is limited (Figure 6h,e), possibly because clear-sky infrared observations from a water vapor channel provide little direct information on boundary-layer moisture.

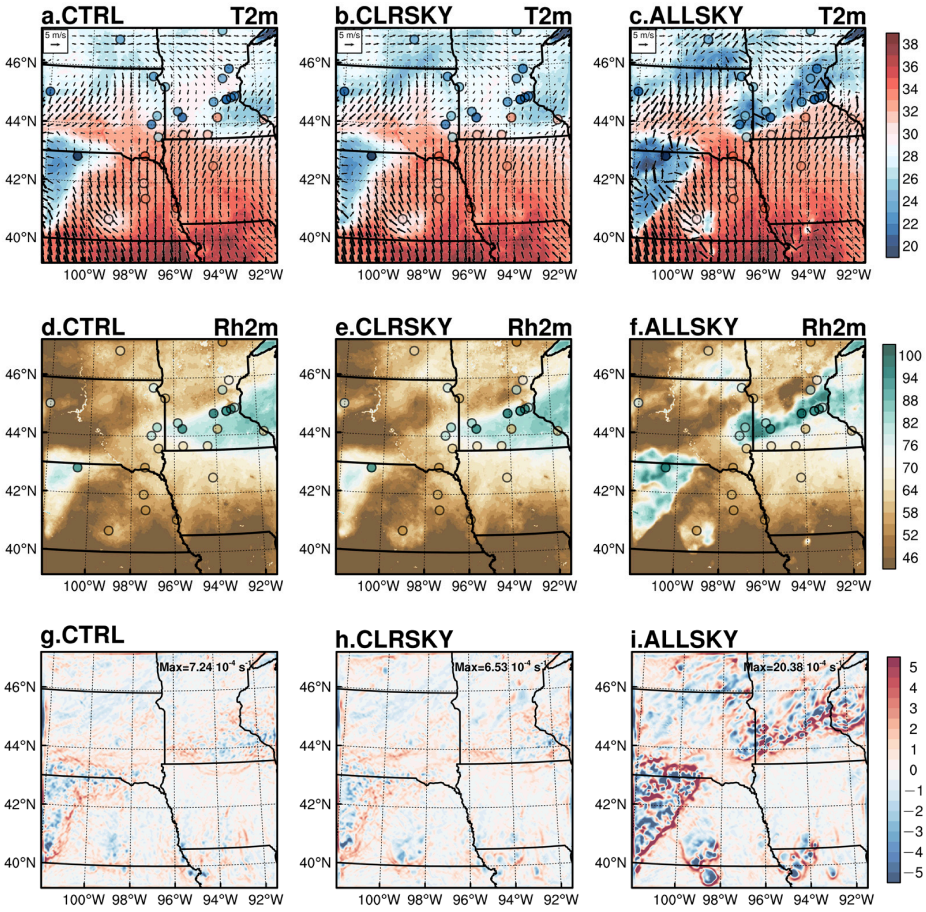


Figure 6. (**a**–**c**) Ensemble-mean 2 m temperature, (**d**–**f**) 2 m relative humidity, and (**g**–**i**) 10 m wind convergency at the final analysis time of 2300 UTC for (**a**,**d**,**g**) CTRL, (**b**,**e**,**h**) CLRSKY, and (**c**,**f**,**i**) ALLSKY. The 10 m wind fields (vectors; m s^{-1}) are overlaid on the ensemble-mean 2 m temperature fields. Colored circles show the corresponding 2 m temperature and relative humidity observations from Automated Surface Observing System stations, respectively.

Table 1. Biases and RMSEs of 2 m temperature (T2) and 2 m relative humidity (RH2) from the CTRL, CLRSKY, and ALLSKY experiments against ASOS observations at 2300 UTC on 12 July 2018.

Experiment Name	T2 Bias (°C)	T2 RMSE (°C)	RH2 Bias (%)	RH2 RMSE (%)
CTRL	2.083	4.112	−5.565	14.041
CLRSKY	1.783	3.707	−5.439	14.119
ALLSKY	1.218	3.062	−3.277	10.335

ALLSKY produces the most accurate analysis of surface temperatures and relative humidity, especially within and around the convective system. The biases of 2 m temperature and relative humidity are reduced to 1.22 °C and −3.28%, while the RMSEs are reduced to 3.06 °C and 10.34%, a reduction of more than 25% relative to CTRL. The assimilation of additional cloudy BTs enhances the evaporative cooling processes, leading to a more pronounced and better-defined cold pool structure. Consistent with this improvement, the maximum 10 m convergence reaches 20.38 $\times$ 10^{-4} s^{-1} in ALLSKY, compared with 7.24 $\times$ 10^{-4} s^{-1} in CTRL. The stronger convergence along the gust front provides a more favorable near-surface environment for initiating new convective cells and maintaining the organization of the MCS.

Overall, the results indicate that all-sky ABI assimilation improves not only the internal cloud structure but also the near-surface meso-scale environment associated with the evolution of target MCS.

4.3. Object-Based Verifications

In this subsection, the object-based verification method described by Skinner et al. [48–51] is applied to evaluate the 0–4 h ensemble and deterministic forecast performance. Three types of objects are examined, including the clear-sky environment characterized by ABI channel 10 BTs, high cloud-top structures characterized by ABI channel 14 BTs, and precipitation structures derived from composite radar reflectivity. The thresholds used to define these objects follow previous studies [50–52], including BT10 > 250 K, BT14 < 216 K, and radar reflectivity exceeding 20 and 40 dBZ.

The ensemble probabilities of the two radar-derived objects from each experiment are first examined subjectively (Figure 7). It is seen that, for the 20 dBZ threshold, all three experiments successfully capture the overall orientation of the target MCS from Nebraska to South Dakota. CTRL consistently produces the lowest ensemble probabilities and develops widespread spurious precipitation over southern Minnesota at 0200 and 0300 UTC. CLRSKY predicts slightly higher ensemble probabilities for the system from Nebraska to South Dakota, with areas exceeding 0.7 being more extensive, particularly during 0200 and 0300 UTC. Meantime, CLRSKY shows a slight reduction in spurious precipitation over southern Minnesota at 0100 UTC. However, both CTRL and CLRSKY fail to adequately predict the precipitation from Minnesota to Wisconsin, suggesting that the surrounding environment is still less conducive for convective development. ALLSKY exhibits substantially improved forecast confidence for the 20 dBZ threshold, particularly for the Minnesota-to-Wisconsin convective region. The ensemble probability fields show excellent agreement with the observed precipitation structure, with regions of high probability (p > 0.7) closely matching the observed precipitation regions in both shape and extent. Furthermore, the assimilation of additional cloudy-sky observations effectively reduces spurious precipitation areas within the model domain, indicating more accurate representation of the convective environment.

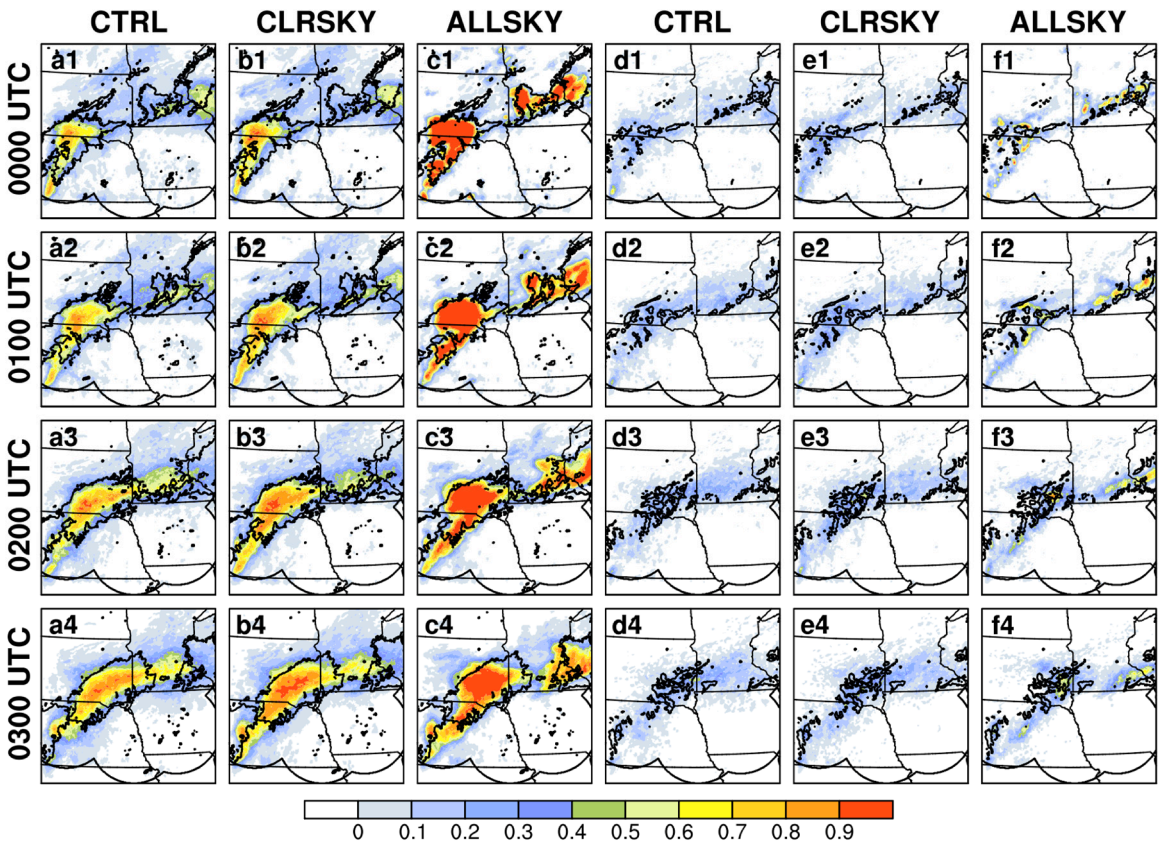


Figure 7. Neighborhood ensemble probabilities (shaded) of composite radar reflectivity exceeding (left three columns) 20 dBZ and (right three columns) 40 dBZ at (**a1**–**f1**) 0000, (**a2**–**f2**) 0100, (**a3**–**f3**) 0200 and (**a4**–**f4**) 0300 UTC for CTRL, CLRSKY and ALLSKY. The region of observed radar reflectivity exceeding certain thresholds is outlined by a bold black contour.

For the threshold of 40 dBZ, CTRL and CLRSKY show similar deficiencies, both significantly underestimating the probability of strong convection through the entire forecast period ($p < 0.4$). ALLSKY successfully predicts multiple convective cores and generally depicts the orientation of the observed convective line. However, these convective cores are somewhat displaced, likely a consequence of both analysis and model errors [53].

Figure 8 quantifies the impact of assimilating ABI BTs on the deterministic composite reflectivity forecasts. Two neighborhood radii of 15 and 60 km are selected to evaluate forecast skill under storm-scale and meso-scale spatial tolerances, respectively. For the 20 dBZ threshold, ALLSKY maintains higher neighborhood ETSs than CTRL and CLRSKY throughout the forecast at both neighborhood radii. The advantage is larger for the 15 km neighborhood, for which the ALLSKY scores remain generally around 0.4, whereas the ETSs of CTRL and CLRSKY are mostly below 0.27. The ETSs decrease for the 60 km neighborhood in all three experiments. For the 40 dBZ threshold, the ETSs increase with forecast lead time as the observed and simulated convective systems develop. ALLSKY again shows the highest scores, with its ETS reaching approximately 0.6 during the later forecast period at the 60 km radius. The ETSs of CTRL and CLRSKY show similar variation and increase gradually with forecast time. The stronger improvement at 60 km for the 40 dBZ threshold indicates that ALLSKY better captures the occurrence and evolution of intense convective echoes, although displacement errors remain at smaller spatial scales.

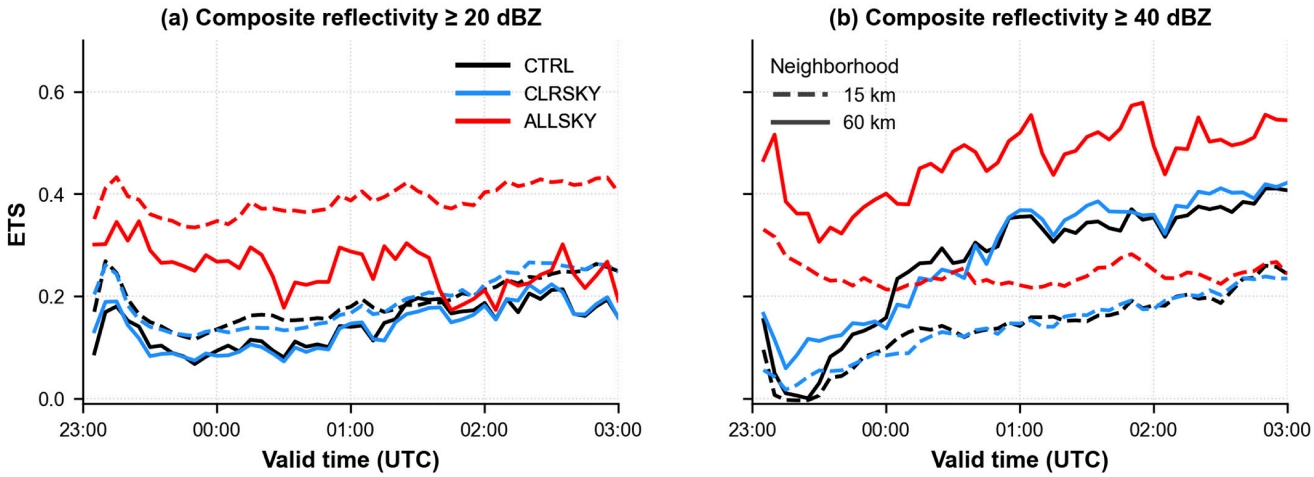


Figure 8. Neighborhood equitable threat scores (NETSs) for objects derived from (**a**) 20 dBZ and (**b**) 40 dBZ composite reflectivity in the CTRL (black), CLRSKY (blue), and ALLSKY (red) experiments during the 4 h deterministic forecasts. Neighborhood radii of 15 km (dashed lines) and 60 km (solid lines) are selected.

Similarly, we calculate the ETSs from the CTRL, CLRSKY, and ALLSKY experiments for the BT-derived objects (Figure 9). For the Channel 10 clear-sky object, CLRSKY outperforms CTRL primarily during the first 1.5 h of the forecast, although the absolute improvement is generally less than 0.05. This advantage diminishes with increasing forecast time, and both experiments exhibit similar ETSs of approximately 0.27 by 0300 UTC. For the Channel 14 cold cloud object, CLRSKY shows no obvious improvement over CTRL in the first 2 h, but its superiority gradually emerges after 0100 UTC. The ETS increases from approximately 0.2 in CTRL to 0.3 in CLRSKY at 0300 UTC for channel 14 object. The evolution of the ETSs in CLRSKY suggests that the early improvements in the MCS environment obtained by clear-sky radiance assimilation contribute to the subsequent organization and intensification of convection. For both BT-derived objects, ALLSKY has the highest ETSs throughout the entire 4 h forecast, maintaining values over 0.5 and 0.4 for Channel 10 and 14, respectively. This persistent superiority implies additional constraints on both the MCS environment and deep convective cloud structure.

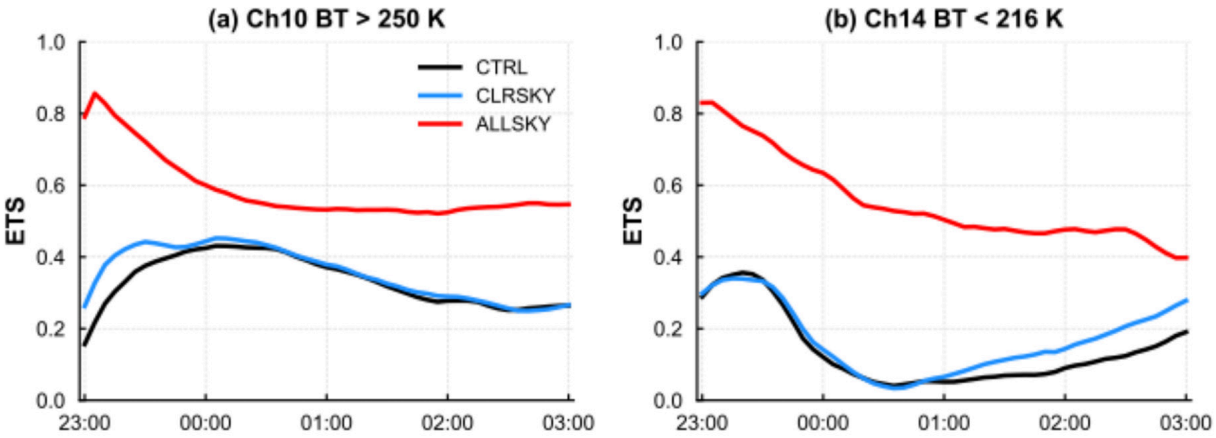


Figure 9. Equitable threat scores (ETSs) for objects derived from (**a**) ABI Channel 10 BTs greater than 250 K and (**b**) Channel 14 BTs less than 216 K during the 4 h deterministic forecasts.

To provide a more comprehensive assessment of the performance of different experiments, the forecasts of the satellite- and radar-derived objects at 1 h and 4 h lead times are further quantitatively verified by the performance diagrams (Figure 10). The diagrams sum-

marize both the deterministic forecasts (large symbols) and individual ensemble members (small symbols) for CTRL, CLRSKY and ALLSKY. Forecasts located closer to the upper-right corner indicate higher forecast skill, corresponding to higher probability of detection (POD), higher success ratio (SR), larger critical success index (CSI), and a frequency bias closer to one.

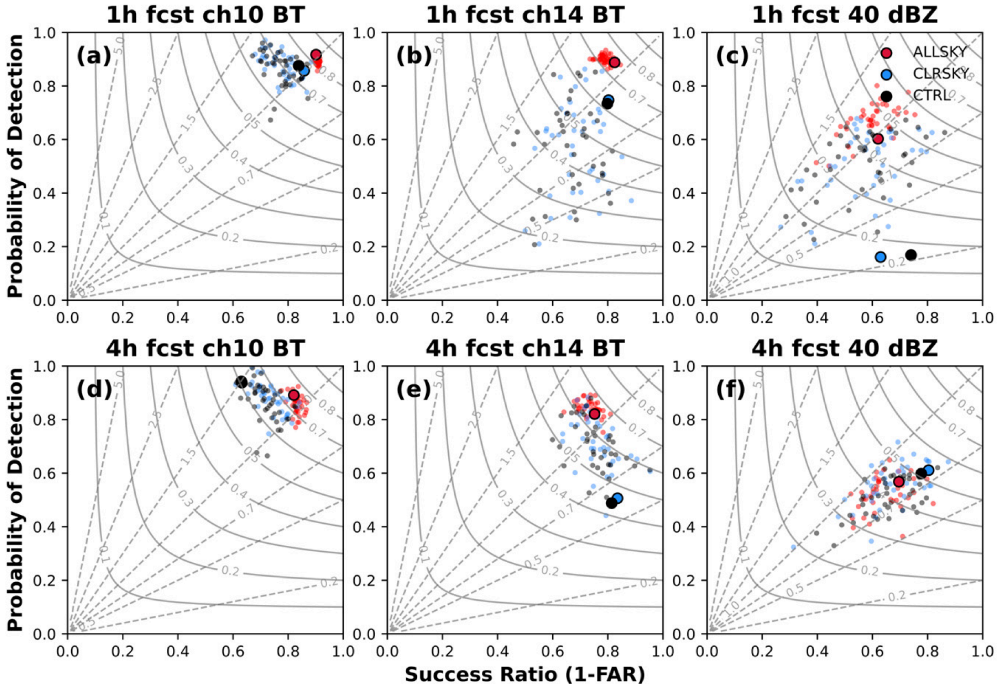


Figure 10. Performance diagrams for (**a**,**d**) ABI Channel 10, (**b**,**e**) ABI Channel 14 and (**c**,**f**) 40 dBZ radar reflectivity objects in the CTRL (black), CLRSKY (blue), and ALLSKY (red) forecasts at (**a**–**c**) 1 and (**d**–**f**) 4 h lead times. Large symbols represent deterministic forecasts, and small symbols represent individual ensemble members.

For both BT-derived objects, ALLSKY generally exhibits frequency biases closest to unity, and also the highest CSIs. Specifically, for the channel 10 BT object, both CTRL and CLRSKY systematically overpredict the coverage of the observed clear-sky regions, leading to much smaller SRs. This is particularly evident for the deterministic forecasts at 4 h. For Channel 14, the improvement in ALLSKY is primarily associated with its higher PODs, which indicate that ALLSKY captures a substantially larger fraction of the observed cold cloud tops. CLRSKY outperforms CTRL by slightly increasing the POD and SR values at the same time. For the 40 dBZ object, ALLSKY shows the highest PODs while maintaining SRs comparable to CLRSKY at 1 h leading time. Although CTRL occasionally exhibits higher SR than ALLSKY in the deterministic forecast, its considerably lower PODs indicate underestimation of the intense convective echoes. At 4 h, the advantage of ALLSKY is not evident, likely due to the displacement errors of the forecast convective cores (Figure 7). It is also noteworthy that the ensemble members of ALLSKY are more tightly clustered around their corresponding deterministic forecasts, suggesting higher ensemble consistency and smaller forecast uncertainty. The members in CTRL and CLRSKY exhibit substantially larger ensemble spreads.

4.4. Precipitation Impacts

To evaluate the impact of assimilating ABI BTs on precipitation forecasting, we compare the 4 h accumulated precipitation forecasts from CTRL, CLRSKY and ALLSKY initialized from 2300 UTC against the NCEP stage IV precipitation observations. The observed

precipitation shows a clear southeast–northwest oriented distribution (Figure 11a), with two major precipitation areas occurring along the southern South Dakota and eastern Minnesota border, respectively (black boxed regions). CTRL and CLRSKY substantially underestimate both the coverage and intensity of precipitation. In particular, neither experiment reproduces the observed heavy precipitation cores near the Minnesota–Wisconsin border, where their simulated accumulations are predominantly below 5 mm. Compared with CTRL, CLRSKY produces a modest increase in weak precipitation over South Dakota and northern Nebraska but provides little improvement in the eastern precipitation area. ALLSKY shows the best agreement with the observations by producing a more coherent rainband distribution. Particularly, ALLSKY successfully reproduces the localized precipitation cores exceeding 50 mm in both boxed regions, including the precipitation near the Minnesota border that is largely missing from CTRL and CLRSKY.

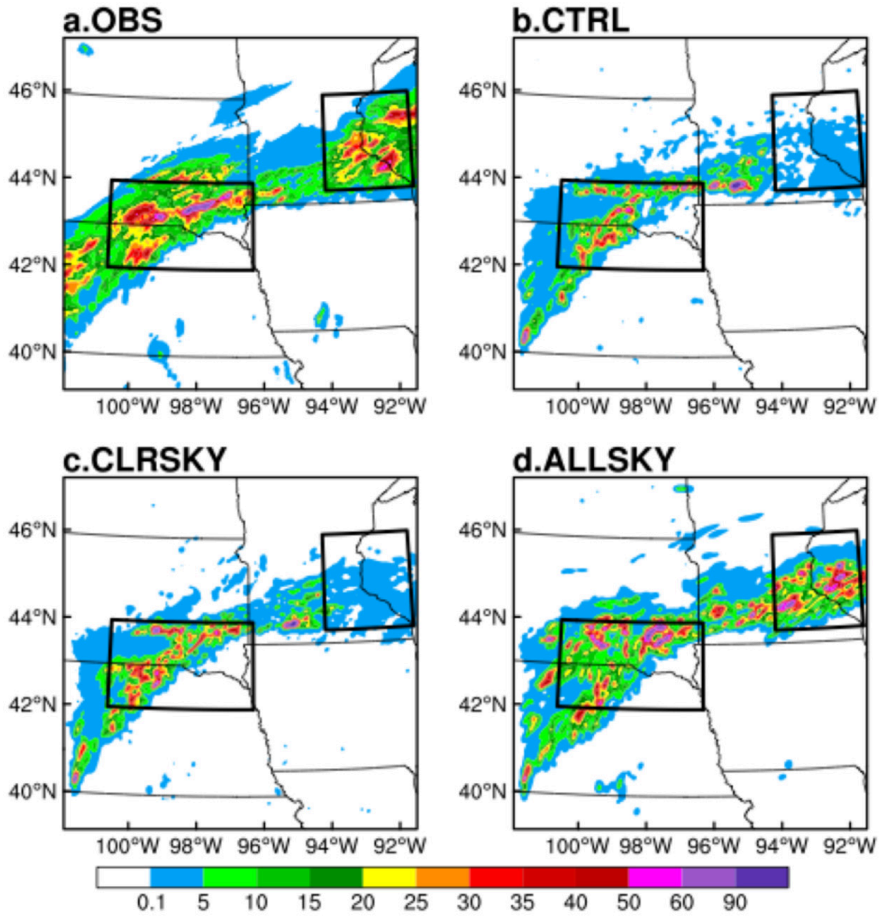


Figure 11. 4 h accumulated precipitation forecasts initialized from 2300 UTC, 12 July, to 0300 UTC, 13 July, 2018 for (**a**) NCEP Stage IV observations and the (**b**) CTRL, (**c**) CLRSKY, and (**d**) ALLSKY experiments. The black boxes denote regions with heavy observed precipitation.

The forecast performance is further quantitatively assessed using the neighborhood-based fractions skill score (FSS) [54]. Figure 12 presents the FSSs of the 4 h accumulated precipitation forecasts from CTRL, CLRSKY, and ALLSKY at different precipitation thresholds, using neighborhood radii of 9, 15, and 30 km. For all experiments, the FSS generally decreases with increasing precipitation threshold but increases with neighborhood radius. CTRL has the lowest FSSs for almost all thresholds and neighborhood radii. CLRSKY provides modest improvements over CTRL, with absolute FSS increases ranging from 0.02 to 0.13 for thresholds below 30 mm. However, for the 50 mm threshold, CLRSKY provides limited improvement over CTRL and even shows a lower FSS at a radius of 30 km. ALLSKY

significantly increases the FSSs for all thresholds and neighborhood radii. For example, ALLSKY increases the FSS relative to CTRL by 0.215, 0.349, 0.380, 0.220, 0.173, and 0.163 at thresholds of 1, 5, 10, 20, 30, and 50 mm, respectively, when using a neighborhood radius of 15 km. These results highlight the positive impact of all-sky infrared radiance assimilation on forecasting both the spatial extent and intensity of MCS-related precipitation.

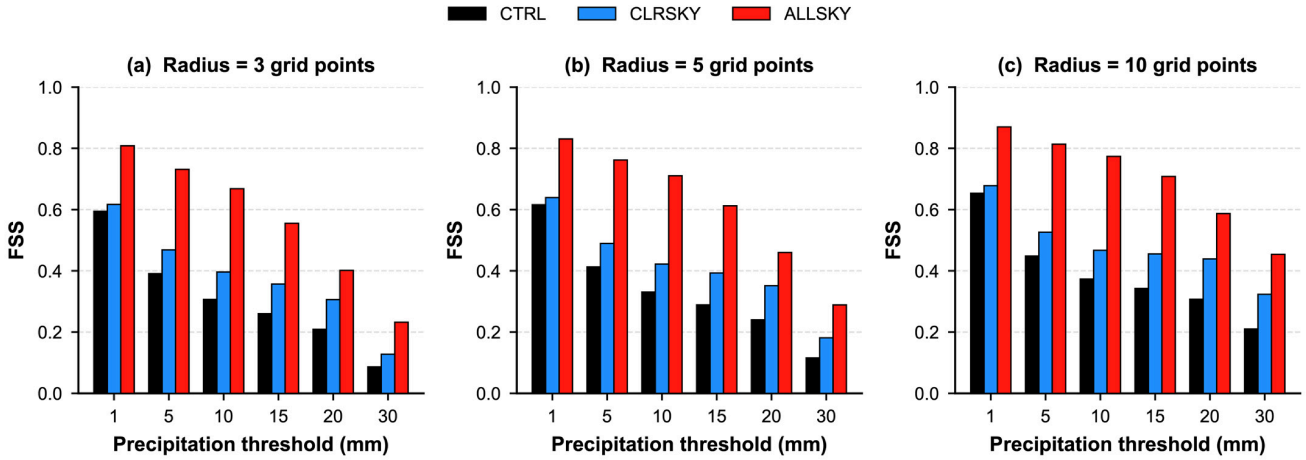


Figure 12. Fractions skill scores (FSSs) of 4 h accumulated precipitation forecasts from CTRL (black), CLRSKY (blue), and ALLSKY (red) at thresholds of 1, 5, 10, 20, 30, and 50 mm. The FSSs are calculated against NCEP Stage IV precipitation analyses using circular neighborhood radii of (**a**) 3, (**b**) 5, and (**c**) 10 grid points, corresponding to approximately 9, 15, and 30 km, respectively.

Nevertheless, noticeable errors remain in the location and structure of the precipitation. The heavy-rainfall cores are generally less organized than observed, and several spurious precipitation maxima are produced (Figure 11d). These remaining deficiencies may be partly attributed to the inherent limitations of infrared radiance observations, which are primarily sensitive to cloud-top properties. While the assimilation of all-sky infrared radiances can improve the representation of deep convective clouds, it provides only indirect constraints on the underlying precipitation and hydrometeor structures.

5. Discussion

Assimilation of all-sky infrared radiances from ABI Channel 10 provides additional information that is unavailable from clear-sky assimilation, and substantially improves the analysis and short-range forecast of the MCS examined in this study. The major findings are broadly consistent with previous comparison studies of clear-sky and all-sky IR DA using advanced geostationary imagers [21,28,31,32]. A common conclusion is that all-sky IR DA effectively improves analyzed and forecast cloud fields, and provides more pronounced analysis increments than clear-sky DA owing to the greater spatial and temporal coverage.

The reported precipitation improvement, however, varies among previous studies. In Okamoto et al. [21], although all-sky assimilation produced a more stable forecast of an organized rainfall event than clear-sky assimilation, the improvement in precipitation ETS was not statistically significant. Similar conclusions were achieved by Xu et al. [31] for a Severe Storm case over North China. More recent EnKF studies on warm-sector heavy rainfall have reported stronger quantitative precipitation benefits. For example, Lou et al. [55] pointed out that hourly all-sky AHI assimilation increased both precipitation TS (0.2–0.4) and FSS when compared to clear-sky assimilation. He et al. [32] reported corresponding all-sky benefits during the 0–6 h forecast period. These results are broadly consistent with the present study.

The differences among the reported impacts are likely attributed to the distinct error characteristics and spatiotemporal scales of the weather systems examined. The present study focuses on a frontal MCS over the central United States, whereas previous studies have examined organized rainfall systems and warm-sector heavy-rainfall events. For isolated convective storms and MCSs, the smaller scale and rapid growth of position errors may significantly reduce the robustness of cross-variable covariances. In addition, their forecast skill can be strongly affected by errors in convective initiation. Warm-sector rainfall is often sustained by boundary-layer moisture convergence, low-level jets, and warm-cloud processes. The impact obtained for a single MCS case should therefore not be generalized to all convective systems, and systematic evaluation over additional cases is required.

Several other limitations should also be considered when interpreting the results. First of all, ALLSKY successfully predicted convection over Minnesota that was largely absent in CTRL and CLRSKY, but the simulated deep convective cores exhibited noticeable displacement errors. Because infrared observations cannot penetrate thick clouds, they provide limited direct constraints on both boundary-layer conditions and vertical structure of hydrometeors. Residual errors in these fields may affect subsequent convective initiation and organization. Errors in the large-scale environmental forcing also influence the evolution of the simulated convection. Forecast model errors, particularly those associated with cloud microphysics, also significantly affect the persistence of the assimilation impact. The present experiments use WRF-ARW version 3.8.1 with the Thompson microphysics scheme, which does not eliminate systematic model errors. Experiments using updated model configurations and multiple microphysics schemes are needed. Secondly, only ABI Channel 10 was assimilated in this study. This water vapor channel is sensitive to the moisture in the lower to middle troposphere, but offers limited information at the boundary layer. Assimilation of multiple ABI channels, together with radar and conventional observations, may provide more complete vertical and microphysical information. Thirdly, the fixed bias correction applied here does not explicitly represent biases associated with air mass, scan geometry, surface properties, or cloud conditions. More advanced cloud-dependent bias correction, vertical localization, and observation-error models, including approaches proposed by Otkin et al. [44] and Feng and Pu [46], should be investigated to better address systematic and non-Gaussian errors in all-sky infrared radiance assimilation.

6. Conclusions

This study compared the impacts of clear-sky and all-sky GOES-16 Advanced Baseline Imager (ABI) infrared radiance assimilation on the analysis and short-range forecast of a meso-scale convective system (MCS). A continental MCS that occurred over the central United States on 12 July 2018 was selected as the case study. Three rapid-cycling experiments were conducted using an ensemble Kalman filter (EnKF) within a 3 km convection-permitting model, including a control experiment without data assimilation (CTRL), a clear-sky assimilation experiment (CLRSKY), and an all-sky assimilation experiment (ALLSKY).

To assimilate clear-sky ABI radiances, we first developed a six-step quality-control scheme based on the GSI EnKF framework. The results showed that the newly established QC scheme effectively removed observations with large innovations, providing a more Gaussian distribution of the innovations. Observation-space diagnostics showed that assimilating either clear-sky or all-sky ABI radiances reduced the mean bias and root-mean-square error of ABI BTs. CLRSKY partially suppressed the spurious clouds in the model background, whereas ALLSKY exhibited superior performance in the analysis of the cloud field.

CLRSKY primarily adjusted the temperature and moisture in the near-storm environment. These adjustments can further modify the vertical distributions of hydrometeors during model integration, thereby improving the forecast of radar reflectivity. ALLSKY directly constrained the hydrometeor fields and produced in-storm thermodynamic and circulation structures more favorable for MCS development and intensification. CLRSKY produced only a small improvement in the analyzed near-surface environment, whereas ALLSKY generated a stronger and more clearly defined cold-pool signature. The resulting surface temperature and humidity fields showed closer agreement with the available station observations.

Object-based verification further showed that CLRSKY improved the Channel 10 BT forecasts during the early forecast period and the subsequent Channel 14 BT forecasts. In contrast, the improvements of ALLSKY persisted for at least 4 h. Compared with both the no-DA control and CLRSKY, ALLSKY had an overall positive impact on the forecast location and intensity of precipitation.

Author Contributions: Conceptualization, L.Z. and M.X.; methodology, L.Z.; validation, L.Z.; writing—original draft preparation, L.Z.; writing—review and editing, M.X. and H.L.; visualization, L.Z.; supervision, M.X. and H.L.; project administration, H.L. and J.L. All authors have read and agreed to the published version of the manuscript.

Funding: This research was primarily funded by the National Natural Science Foundation of China, Grant No. 42475168; the Science and Technology Commission of Shanghai Municipality, Grant No. 24QA2709000 and the National Key Research and Development Program of China, Grant No. 2022YFC3080500.

Data Availability Statement: The original data presented in the study are openly available in Harvard Dataverse at: https://doi.org/10.7910/DVN/1B7KG8 (accessed on 20 August 2026).

Acknowledgments: The NSF Extreme Science and Engineering Discovery Environment (XSEDE) supercomputing resources at the Texas Advanced Computing Center were used for most of the DA experiments. The authors thank the two anonymous reviewers for their constructive comments and suggestions, which helped improve the manuscript. The authors have reviewed and edited the output and take full responsibility for the content of this publication.

Conflicts of Interest: The authors declare no conflicts of interest.

References

1. Yano, J.-I.; Ziemiański, M.Z.; Cullen, M.; Termonia, P.; Onvlee, J.; Bengtsson, L.; Carrassi, A.; Davy, R.; Deluca, A.; Gray, S.L.; et al. Scientific Challenges of Convective-Scale Numerical Weather Prediction. *Bull. Am. Meteorol. Soc.* **2018**, *99*, 699–710. [CrossRef]
2. Houze, R.A. 100 Years of Research on Mesoscale Convective Systems. *Meteorol. Monogr.* **2018**, *59*, 17.11–17.54. [CrossRef]
3. Gustafsson, N.; Janjić, T.; Schraff, C.; Leuenberger, D.; Weissmann, M.; Reich, H.; Brousseau, P.; Montmerle, T.; Wattrelot, E.; Bučánek, A.; et al. Survey of data assimilation methods for convective-scale numerical weather prediction at operational centres. *Q. J. R. Meteorol. Soc.* **2018**, *144*, 1218–1256. [CrossRef]
4. Zhang, F.; Snyder, C.; Rotunno, R. Effects of moist convection on mesoscale predictability. *J. Atmos. Sci.* **2003**, *60*, 1173–1185. [CrossRef]
5. Judt, F. Insights into Atmospheric Predictability through Global Convection-Permitting Model Simulations. *J. Atmos. Sci.* **2018**, *75*, 1477–1497. [CrossRef]
6. Majumdar, S.J.; Sun, J.; Golding, B.; Joe, P.; Dudhia, J.; Caumont, O.; Chandra Gouda, K.; Steinle, P.; Vincendon, B.; Wang, J.; et al. Multiscale Forecasting of High-Impact Weather: Current Status and Future Challenges. *Bull. Am. Meteorol. Soc.* **2021**, *102*, E635–E659. [CrossRef]
7. Zou, X.L.; Qin, Z.K.; Weng, F.Z. Improved Coastal Precipitation Forecasts with Direct Assimilation of GOES-11/12 Imager Radiances. *Mon. Weather Rev.* **2011**, *139*, 3711–3729. [CrossRef]
8. Qin, Z.K.; Zou, X.L.; Weng, F.Z. Evaluating Added Benefits of Assimilating GOES Imager Radiance Data in GSI for Coastal QPFs. *Mon. Weather Rev.* **2013**, *141*, 75–92. [CrossRef]

9. Szyndel, M.D.E.; Kelly, G.; Thépaut, J.N. Evaluation of potential benefit of assimilation of SEVIRI water vapour radiance data from Meteosat-8 into global numerical weather prediction analyses. *Atmos. Sci. Lett.* **2005**, *6*, 105–111. [CrossRef]
10. Hersbach, H.; Bell, B.; Berrisford, P.; Hirahara, S.; Horányi, A.; Muñoz-Sabater, J.; Nicolas, J.; Peubey, C.; Radu, R.; Schepers, D.; et al. The ERA5 global reanalysis. *Q. J. R. Meteorol. Soc.* **2020**, *146*, 1999–2049. [CrossRef]
11. Yang, C.; Liu, Z.; Gao, F.; Childs, P.P.; Min, J. Impact of assimilating GOES imager clear-sky radiance with a rapid refresh assimilation system for convection-permitting forecast over Mexico. *J. Geophys. Res. Atmos.* **2017**, *122*, 5472–5490. [CrossRef]
12. Wang, Y.; Liu, Z.; Yang, S.; Min, J.; Chen, L.; Chen, Y.; Zhang, T. Added Value of Assimilating Himawari-8 AHI Water Vapor Radiances on Analyses and Forecasts for "7.19" Severe Storm Over North China. *J. Geophys. Res. Atmos.* **2018**, *123*, 3374–3394. [CrossRef]
13. Hutt, A.; Schraff, C.; Anlauf, H.; Bach, L.; Baldauf, M.; Bauernschubert, E.; Cress, A.; Faulwetter, R.; Fundel, F.; Köpken-Watts, C.; et al. Assimilation of SEVIRI Water Vapor Channels With an Ensemble Kalman Filter on the Convective Scale. *Front. Earth Sci.* **2020**, *8*, 70. [CrossRef]
14. Ma, Z.; Maddy, E.S.; Zhang, B.; Zhu, T.; Boukabara, S.A. Impact Assessment of Himawari-8 AHI Data Assimilation in NCEP GDAS/GFS with GSI. *J. Atmos. Ocean. Technol.* **2017**, *34*, 797–815. [CrossRef]
15. Ballard, S.P.; Li, Z.; Simonin, D.; Caron, J.-F. Performance of 4D-Var NWP-based nowcasting of precipitation at the Met Office for summer 2012. *Q. J. R. Meteorol. Soc.* **2016**, *142*, 472–487. [CrossRef]
16. Wu, Y.; Liu, Z.; Li, D. Improving forecasts of a record-breaking rainstorm in Guangzhou by assimilating every 10-min AHI radiances with WRF 4DVAR. *Atmos. Res.* **2020**, *239*, 104912. [CrossRef]
17. Zhang, F.; Minamide, M.; Clothiaux, E.E. Potential impacts of assimilating all-sky infrared satellite radiances from GOES-R on convection-permitting analysis and prediction of tropical cyclones. *Geophys. Res. Lett.* **2016**, *43*, 2954–2963. [CrossRef]
18. Zhang, Y.; Zhang, F.; Stensrud, D.J. Assimilating All-Sky Infrared Radiances from GOES-16 ABI Using an Ensemble Kalman Filter for Convection-Allowing Severe Thunderstorms Prediction. *Mon. Weather Rev.* **2018**, *146*, 3363–3381. [CrossRef]
19. Honda, T.; Miyoshi, T.; Lien, G.-Y.; Nishizawa, S.; Yoshida, R.; Adachi, S.A.; Terasaki, K.; Okamoto, K.; Tomita, H.; Bessho, K. Assimilating All-Sky Himawari-8 Satellite Infrared Radiances: A Case of Typhoon Soudelor (2015). *Mon. Weather Rev.* **2018**, *146*, 213–229. [CrossRef]
20. Minamide, M.; Zhang, F. Assimilation of All-Sky Infrared Radiances from Himawari-8 and Impacts of Moisture and Hydrometer Initialization on Convection-Permitting Tropical Cyclone Prediction. *Mon. Weather Rev.* **2018**, *146*, 3241–3258. [CrossRef]
21. Okamoto, K.; Sawada, Y.; Kunii, M. Comparison of assimilating all-sky and clear-sky infrared radiances from Himawari-8 in a mesoscale system. *Q. J. R. Meteorol. Soc.* **2019**, *145*, 745–766. [CrossRef]
22. Zhu, L.; Xue, M.; Kong, R.; Min, J. Direct Assimilation of All-Sky GOES-R ABI Radiances in GSI EnKF for the Analysis and Forecasting of a Mesoscale Convective System. *Mon. Weather Rev.* **2023**, *151*, 737–760. [CrossRef]
23. Kim, Y.-S.; Wang, X.; Johnson, A. Impact of Microphysics Parameterization Schemes on the Assimilation of GOES-16 ABI All-Sky Infrared Radiances for a Bow Echo Analysis and Prediction. *J. Geophys. Res. Atmos.* **2024**, *129*, e2023JD040046. [CrossRef]
24. Johnson, A.; Wang, X.; Jones, T. Impacts of Assimilating GOES-16 ABI Channels 9 and 10 Clear Air and Cloudy Radiance Observations With Additive Inflation and Adaptive Observation Error in GSI-EnKF for a Case of Rapidly Evolving Severe Supercells. *J. Geophys. Res. Atmos.* **2022**, *127*, e2021JD036157. [CrossRef]
25. Schomburg, A.; Schraff, C.; Köpken-Watts, C.; Stephan, K.; Schühl, L.; Faulwetter, R. Operational all-sky assimilation of geostationary infrared water-vapour channels in the regional ICON-D2 model with an ensemble Kalman filter. *Q. J. R. Meteorol. Soc.* **2026**, *152*, e70113. [CrossRef]
26. Rendon, J.; Zhang, Y. Impact of Microphysical Parameterizations on Satellite All-Sky Infrared Data Assimilation and Practical Predictability of Hurricane Harvey (2017). *J. Geophys. Res. Atmos.* **2025**, *130*, e2024JD042697. [CrossRef]
27. Geer, A.J.; Migliorini, S.; Matricardi, M. All-sky assimilation of infrared radiances sensitive to mid- and upper-tropospheric moisture and cloud. *Atmos. Meas. Tech.* **2019**, *12*, 4903–4929. [CrossRef]
28. Okamoto, K.; Ishibashi, T.; Okabe, I. All-sky infrared radiance assimilation of a geostationary satellite in the Japan Meteorological Agency's global system. *Q. J. R. Meteorol. Soc.* **2023**, *149*, 2477–2503. [CrossRef]
29. Niu, Z.; Tang, F.; Wang, L. All-sky assimilation of FY-4A AGRI water vapor channels: An observing system experiment study for south Asian monsoon prediction. *Q. J. R. Meteorol. Soc.* **2024**, *150*, 2458–2471. [CrossRef]
30. Yang, C.; Zhong, T.; Min, J. A preliminary study of FY-4B AGRI all-sky assimilation by WRFDA for tropical cyclones. *Atmos. Res.* **2026**, *327*, 108377. [CrossRef]
31. Xu, D.; Liu, Z.; Fan, S.; Chen, M.; Shen, F. Assimilating all-sky infrared radiances from Himawari-8 using the 3DVar method for the prediction of a severe storm over North China. *Adv. Atmos. Sci.* **2021**, *38*, 661–676. [CrossRef]
32. He, J.; Ding, W.; Wang, H.; Xiao, H.; Chen, S.; Zhang, H.; Deng, H.; Ma, X. Pilot EnKF assimilation of FY-4A AGRI All-sky upper-tropospheric water vapor radiances for a warm-sector heavy rainfall case in South China. *Atmos. Res.* **2026**, *337*, 108934. [CrossRef]

33. Skamarock, W.C.; Klemp, J.B.; Dudhia, J.; Gill, D.O.; Barker, D.; Duda, M.G.; Huang, X.Y.; Wang, W.; Powers, J.G. *A description of the Advanced Research WRF Version 3*; NCAR Tech. Note NCAR/TN-475 + STR; National Center for Atmospheric Research: Boulder, CO, USA, 2008; 113p.
34. Han, Y.; Delst, P.v.; Liu, Q.; Weng, F.; Yan, B.; Treadon, R.; Derber, J. *JCSDA Community Radiative Transfer Model (CRTM): Version 1*; NOAA Technical Report NESDIS 122; NESDIS: Silver Spring, MD, USA, 2006; 40p.
35. Kong, R.; Xue, M.; Fierro, A.O.; Jung, Y.; Liu, C.; Mansell, E.R.; MacGorman, D.R. Assimilation of GOES-16 geostationary lightning mapper flash extent density data in GSI EnKF for the analysis and short-term forecast of a mesoscale convective system. *Mon. Weather Rev.* **2020**, *148*, 2111–2133. [CrossRef]
36. Thompson, G.; Field, P.R.; Rasmussen, R.M.; Hall, W.D. Explicit forecasts of winter precipitation using an improved bulk microphysics scheme. Part II: Implementation of a new snow parameterization. *Mon. Weather Rev.* **2008**, *136*, 5095–5115. [CrossRef]
37. Hong, S.-Y.; Noh, Y.; Dudhia, J. A new vertical diffusion package with an explicit treatment of entrainment processes. *Mon. Weather Rev.* **2006**, *134*, 2318–2341. [CrossRef]
38. Iacono, M.J.; Delamere, J.S.; Mlawer, E.J.; Shephard, M.W.; Clough, S.A.; Collins, W.D. Radiative forcing by long-lived greenhouse gases: Calculations with the AER radiative transfer models. *J. Geophys. Res. Atmos.* **2008**, *113*, D13103. [CrossRef]
39. Chen, F.; Dudhia, J. Coupling an Advanced Land Surface-Hydrology Model with the Penn State-NCAR MM5 Modeling System. Part I: Model Implementation and Sensitivity. *Mon. Weather Rev.* **2001**, *129*, 569. [CrossRef]
40. Zhang, F.; Snyder, C.; Sun, J. Impacts of initial estimate and observations on the convective-scale data assimilation with an ensemble Kalman filter. *Mon. Weather Rev.* **2004**, *132*, 1238–1253. [CrossRef]
41. Minamide, M.; Zhang, F. Adaptive Observation Error Inflation for Assimilating All-Sky Satellite Radiance. *Mon. Weather Rev.* **2017**, *145*, 1063–1081. [CrossRef]
42. Cintineo, R.M.; Otkin, J.A.; Jones, T.A.; Koch, S.; Stensrud, D.J. Assimilation of Synthetic GOES-R ABI Infrared Brightness Temperatures and WSR-88D Radar Observations in a High-Resolution OSSE. *Mon. Weather Rev.* **2016**, *144*, 3159–3180. [CrossRef]
43. Degelia, S.K.; Wang, X.; Wang, Y.; Johnson, A. Assimilation of GOES-16 ABI All-Sky Radiance Observations in RRFS Using EnVar: Methodology, System Development, and Impacts for a Severe Convective Event. *Mon. Weather Rev.* **2023**, *151*, 2739–2758. [CrossRef]
44. Otkin, J.A.; Potthast, R.; Lawless, A.S. Nonlinear Bias Correction for Satellite Data Assimilation Using Taylor Series Polynomials. *Mon. Weather Rev.* **2018**, *146*, 263–285. [CrossRef]
45. Otkin, J.A.; Potthast, R. Assimilation of All-Sky SEVIRI Infrared Brightness Temperatures in a Regional-Scale Ensemble Data Assimilation System. *Mon. Weather Rev.* **2019**, *147*, 4481–4509. [CrossRef]
46. Feng, C.; Pu, Z. A Bias Correction Scheme with the Symmetric Cloud Proxy Variable and Its Influence on Assimilating All-Sky GOES-16 Brightness Temperatures. *Mon. Weather Rev.* **2022**, *150*, 3305–3323. [CrossRef]
47. Houze, R.A., Jr. Mesoscale convective systems. *Rev. Geophys.* **2004**, *42*, RG4003. [CrossRef]
48. Skinner, P.S.; Wicker, L.J.; Wheatley, D.M.; Knopfmeier, K.H. Application of Two Spatial Verification Methods to Ensemble Forecasts of Low-Level Rotation. *Weather Forecast.* **2016**, *31*, 713–735. [CrossRef]
49. Skinner, P.S.; Wheatley, D.M.; Knopfmeier, K.H.; Reinhart, A.E.; Choate, J.J.; Jones, T.A.; Creager, G.J.; Dowell, D.C.; Alexander, C.R.; Ladwig, T.T.; et al. Object-Based Verification of a Prototype Warn-on-Forecast System. *Weather Forecast.* **2018**, *33*, 1225–1250. [CrossRef] [PubMed]
50. Jones, T.A.; Wang, X.; Skinner, P.; Johnson, A.; Wang, Y. Assimilation of GOES-13 Imager Clear-Sky Water Vapor (6.5 μm) Radiances into a Warn-on-Forecast System. *Mon. Weather Rev.* **2018**, *146*, 1077–1107. [CrossRef]
51. Jones, T.A.; Skinner, P.; Yussouf, N.; Knopfmeier, K.; Reinhart, A.; Wang, X.; Bedka, K.; Smith, W., Jr.; Palikonda, R. Assimilation of GOES-16 radiances and retrievals into the Warn-on-Forecast system. *Mon. Weather Rev.* **2020**, *148*, 1829–1859. [CrossRef]
52. Griffin, S.M.; Otkin, J.A.; Rozoff, C.M.; Sieglaff, J.M.; Cronce, L.M.; Alexander, C.R.; Jensen, T.L.; Wolff, J.K. Seasonal Analysis of Cloud Objects in the High-Resolution Rapid Refresh (HRRR) Model Using Object-Based Verification. *J. Appl. Meteorol. Climatol.* **2017**, *56*, 2317–2334. [CrossRef]
53. Yussouf, N.; Kain, J.S.; Clark, A.J. Short-Term Probabilistic Forecasts of the 31 May 2013 Oklahoma Tornado and Flash Flood Event Using a Continuous-Update-Cycle Storm-Scale Ensemble System. *Weather Forecast.* **2016**, *31*, 957–983. [CrossRef]
54. Roberts, N.M.; Lean, H.W. Scale-selective verification of rainfall accumulations from high-resolution forecasts of convective events. *Mon. Weather Rev.* **2008**, *136*, 78–97. [CrossRef]
55. Lou, S.; Zhu, L.; Qiu, X.-X.; Chen, G.; Yuan, S.; Zhou, S. Impact of EnKF assimilating Himawari-8 all-sky infrared radiance on the forecasting of a warm-sector rainstorm event. *Sci. China Earth Sci.* **2024**, *67*, 3110–3127. [CrossRef]

Disclaimer/Publisher's Note: The statements, opinions and data contained in all publications are solely those of the individual author(s) and contributor(s) and not of MDPI and/or the editor(s). MDPI and/or the editor(s) disclaim responsibility for any injury to people or property resulting from any ideas, methods, instructions or products referred to in the content.